THE JOURNAL OF PHYSICAL CHEMISTRY LETTERS
A JOURNAL OF THE AMERICAN CHEMICAL SOCIETY

pubs.acs.org/JPCL Letter

Three-in-One Strategy to Improve Both Catalytic Activity and Selectivity: Nonconcentric Pd−Au Nanoparticles

Hong Woo Lee,[▽] Euiyoung Jung,[▽] Geun-Ho Han,[▽] Min-Cheol Kim, Donghun Kim, Kwan-Young Lee,* Sang Soo Han,* and Taekyung Yu*

Cite This: *J. Phys. Chem. Lett.* 2021, 12, 11098−11105 Read Online

ACCESS | Metrics & More | Article Recommendations | Supporting Information

ABSTRACT: In direct H_2O_2 synthesis, the Pd−Au alloy was considered as a potential catalyst because of its much better performance compared to the prototype Pd; unfortunately, achieving both high activity and selectivity remains a challenge. Here, we synthesized nonconcentric Pd−Au NPs in which Au domain shells are formed only partially on Pd domain cores and tested them for direct H_2O_2 synthesis. It has three exposed regions of Pd, Au domains, and Pd−Au interfaces in a single NP (hence, a 3-in-1 strategy). Creating nonconcentric forms was demonstrated convincingly by density functional theory calculations. The nonconcentric Pd−Au particles exhibit high and well-balanced performances that are hard to achieve with traditional alloyed Pd−Au. The number of Pd/Au interfaces was found to be the key factor and thus was optimized by controlling the Au precursor concentrations. The hitherto underutilized structure of nonconcentric bimetallic alloys can be useful and thus should be more actively investigated for catalyst development.

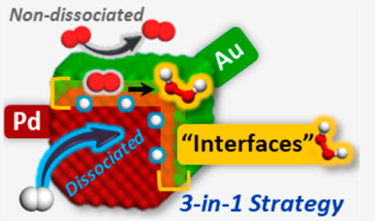

Multimetallic nanoparticles (NPs) are receiving much attention in the field of catalysis because they have various advantages in generating new physicochemical properties that are not observed in monometallic NPs.[1−4] Alloys of two metal elements, in which the elements are homogeneously mixed at the atomic level, can create new electronic structures by orbital coupling and lead to improved catalytic properties.[5−7] Similarly, the strain induced by a lattice mismatch between core and shell metals in core−shell structures can also tune the electronic structure, leading to superior catalytic performance.[4,8,9] For those reasons, alloyed and core−shell NP structures have been mainly considered in the category of bimetallic catalysis; it is imperative to use a new type of bimetallic catalyst.[10,11]

In direct H_2O_2 synthesis from molecular H_2 and O_2, bimetallic catalysts have been heavily explored. In particular, an alloyed Pd−Au NP system has been regarded as a potential catalyst due to its much enhanced performance compared to that of prototypic Pd catalysts.[12−14] In particular, the incorporation of Au into the Pd lattices leads to superior H_2O_2 selectivity,[15] because the Au tends to prevent O_2 dissociation. However, as the content of Au continuously increases on the surface, the active Pd sites gradually disappear. Inevitably, the H_2 conversion capability on the bimetallic catalyst is reduced, thereby lowering H_2O_2 productivity.[15,16] In other words, a trade-off is observed between the catalytic activity and selectivity in Pd−Au alloy nanostructures in H_2O_2 synthesis. Thus, enhancement of both the catalytic activity and selectivity has remained a challenging issue.

Nonconcentric Pd−Au bimetallic NPs, first reported by Zhu et al.,[17] have yet to be explored as catalytic materials; this is the focus of the present study. Nonconcentric Pd−Au NPs are an interesting architecture where Au domain shells are formed only partially on Pd domain cores, although Pd and Au are strongly miscible in the bulk phase.[18] It is well-known that the equilibrium structure of core@shell NPs in which there is lattice mismatch and the small atoms constitute the core is off-centered.[19,20]

The amounts and positions of Au domain shells can be manipulated by controlling the reduction rates, types of reagents, and reaction temperatures. The nonconcentric Pd−Au structures have three exposed regions of Pd domains, Au domains, and Pd−Au interfaces (hence, the 3-in-1 strategy), which implies that three intrinsic properties may synergistically be activated from a single NP structure. The Au domains can offer inactive surface sites resulting from the fully occupied d-bands and thus prevent O_2 dissociation and byproduct formation.[21−24] The Pd domains can facilitate the H_2 conversion process.[24,25] Last, the Pd−Au interfaces can serve as interesting active sites because the Pd domain offers facile H_2 dissociation and the Au domain suppresses O_2 dissociation; therefore, H_2O_2 can be produced at the Pd/Au interfaces. Based on these results, nonconcentric Pd−Au NPs can be considered promising candidates for direct H_2O_2 synthesis, which may lead to high performance in both activity and selectivity. Furthermore, optimizing the three exposure regions

Received: October 5, 2021
Accepted: November 5, 2021

https://doi.org/10.1021/acs.jpclett.1c03256
J. Phys. Chem. Lett. 2021, 12, 11098−11105

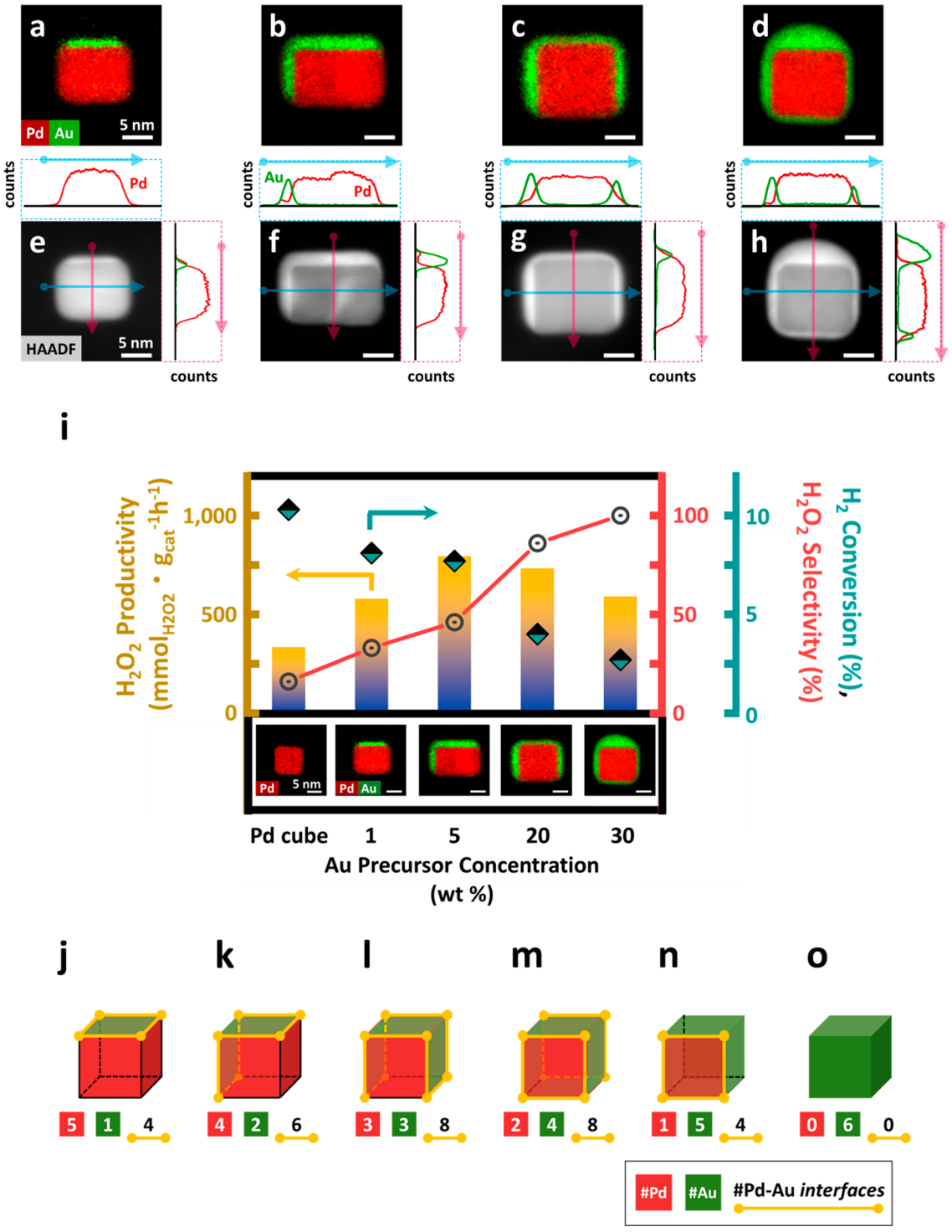

Figure 1. Morphologies of nonconcentric Pd−Au nanoparticles. (a−d) STEM-EDS color mapping analysis (red, Pd; green, Au) of Pd−Au_N NPs with varied concentrations of the Au precursor, in which N = (a, e) 1, (b, f) 5, (c, g) 20, and (d, h) 30 wt %. The white scale bar corresponds to 5 nm. (e−h) High-angle annular dark-field (HAADF) images and line scanned images (red, Pd; green, Au) were recorded along the light-blue and pink arrows on the nonconcentric Pd−Au_N NP images. (i) Catalytic performance of the nonconcentric Pd−Au_N NPs for direct H_2O_2 synthesis. Here, H_2O_2 productivity (navy−yellow bar), selectivity (red line), and H_2 conversion (cyan rhombus symbol) of the Pd−Au_N NPs (N = 1, 5, 20, and 30 wt %) are represented. For comparison, the bare Pd cubes are included. (j−o) Numbers of Pd (red) and Au (green) facets and Pd−Au interfaces (yellow lines) in the Pd−Au_N NPs.

(controlling the ratio of the three exposure regions) is an important challenge.

In this work, to understand the catalytic performance of this new category of bimetallic NP catalysts (namely, nonconcentric NPs), we synthesized nonconcentric Pd−Au NPs based on a previous procedure.[17] The ratio of the three exposed regions (particularly the interfacial area) can be tuned by controlling the Au precursor ($HAuCl_4 \cdot xH_2O$) concentrations. These nonconcentric structures were characterized by transmission electron microscopy (TEM) and energy-dis-

https://doi.org/10.1021/acs.jpclett.1c03256
J. Phys. Chem. Lett. 2021, 12, 11098−11105

persive X-ray spectroscopy (EDS). Using density functional theory (DFT) calculations, the NP nucleation and growth mechanism was also elucidated. The nonconcentric Pd−Au NPs indeed exhibited superior catalytic performance for direct H_2O_2 synthesis that was even hard to achieve with traditional alloyed Pd−Au NPs. We also will discuss that the number of Pd/Au interfaces is a critical factor in determining the catalytic performance of nonconcentric NPs and thus is maximized by controlling the Au precursor concentrations.

We first synthesized Pd nanocube seeds by reducing Na_2PdCl_4 with L-ascorbic acid (AA) in an aqueous solution in the presence of bromide ions (Br^-) as a capping agent and poly(vinyl pyrrolidone) (PVP) as a stabilizer to promote the formation of (100) facets.[26] TEM analyses of the Pd seeds revealed that the Pd cubes had an average diameter of ∼10 nm and exposed six (100) and eight (111) facets (Figure S1, Supporting Information), serving as seeds for the overgrowth of Au atoms. After synthesizing the Pd seeds, we deposited Au layers on them via a direct seed-mediated growth method in which no washing of the seed material was involved. The Au shells were formed in the presence of a residual amount of Br-ion after the formation process of Pd seed. The Br-ion is known as a capping agent involved in the morphology change of Au nanoparticles by attaching to the (100) facets of Au.[27,28] We consider that it is possible that Br-ions may have influenced the formation of Au shells with 100 facets exposed along the 100 facets of Pd in Pd−Au NP synthesis. The amount of Au precursor ($HAuCl_4$) was varied with the ratio of $Na_2PdCl_4/HAuCl_4$ = 100:*X*, where *X* is 1, 5, 20, and 30 wt % in aqueous solutions containing both Pd seeds and AA.

Figure 1a−h shows TEM images of the Pd−Au NPs synthesized by controlling the amounts of the Au precursor. When the amount of Au precursor was 1 wt %, Au layers were grown only on one of the (100) facets of the Pd cubes. As the amount of Au precursor increased, Au layers were deposited on two (5 wt %), three (20 wt %), and four (100) facets (30 wt %) of the Pd cubes. These results indicate that the synthesized Pd−Au NPs indeed have nonconcentric structures, in contrast to previous core@shell Pd@Au structures in which the Au shells fully covered the Pd cores.[29] Although it is difficult to confirm the 3-dimensional structures of the NPs with the 2-dimensional projection images because of the limits of TEM, the clear Au signals in the EDS line scanning analyses indicate that reduced Au atoms are located only on one, two, three, and four (100) facets of the Pd cubes as the amount of the Au precursor increases. Additionally, the wide-angle XRD patterns for the nonconcentric Pd−Au NPs revealed that the shoulder appears at the lower position of the first peak with increasing the Au concentration. This shoulder might be assigned as Au, which supports the formation of nonconcentric Pd−Au. (Figure S2, Supporting Information).

Figure 1i shows the catalytic performance of the nonconcentric Pd−Au_N (*N* = 1, 5, 20, and 30 wt %) NPs supported on SiO_2 for direct H_2O_2 synthesis, in which their H_2 conversion (cyan/black rhombus symbol), H_2O_2 selectivity (red line), and productivity (navy−yellow bar) were evaluated under mild reaction conditions (10 °C, 1 atm). As the Au content in the Pd−Au_N NPs increased, the H_2 conversion decreased from 10.3% with Pd to 2.7% with Pd−Au_{30}, while the H_2O_2 selectivity increased from 16% with Pd to ∼100% with Pd−Au_{30}. To understand the catalytic behavior, we investigated the numbers of Pd and Au domains and Pd−Au interfaces in the Pd−Au NPs, as depicted in Figure 1j−o. As the Au content increased, the number of Pd domains decreased, while that of Au domains increased. Because Au surfaces are inactive for H_2 dissociation, which is necessary for direct H_2O_2 synthesis,[21,24] only the exposed Pd surfaces primarily contributed to the H_2 conversion. Thus, it is understood that the H_2 conversion on Pd−Au NPs decreases with increased Au content. However, the addition of Au onto the Pd enhances selective H_2O_2 synthesis due to the alloying of the Pd and Au atoms.[30,31] At the Pd−Au interfaces in the nonconcentric Pd−Au NPs, Pd and Au atoms can be considered to be alloyed; this topic will be further discussed later. In this regard, the selectivity of the Pd−Au NPs is mainly affected by the Pd−Au interfaces. In Figure 1j−o, the nonconcentric structures with the most Pd−Au interfaces are shown in Figure 1l,m and correspond to Pd−Au_{20} and Pd−Au_{30} NPs, respectively. Although the two structures have the same number of Pd−Au interfaces, the selectivity is likely determined more by the ratio of the interfaces to Pd domains because the Pd−Au interfaces can provide higher selectivity than the Pd domains. Comparing the ratios (8/2 = 4 for Pd−Au_{30} and 8/3 = ∼2.7 for Pd−Au_{20}), one can understand why Pd−Au_{30} provides higher H_2O_2 selectivity. In addition, because H_2O_2 productivity is governed by both H_2 conversion and H_2O_2 selectivity, the highest H_2O_2 productivity (794 $mmol_{H_2O_2}$ g_{metal}^{-1} h^{-1}) is observed for the Pd−Au_5.

The catalytic performance of the nonconcentric Pd−Au NPs was also compared with those of Pd cube, Pd@Au core@shell, and alloyed $Pd_{50}Au_{50}$ NPs synthesized by previously reported procedures;[32,33] the results are summarized in Table S1 of the Supporting Information. The $Pd_{50}Au_{50}$ composition as a representative of the alloyed NPs was chosen because this composition has the best catalytic performance according to a previous report.[33] The Pd nanocubes show high H_2 coverage (10.3%) but low H_2O_2 selectivity (16%). The low selectivity is improved to 88% with the alloyed $Pd_{50}Au_{50}$ NPs, although their H_2 conversion significantly decreases to 3.1%. However, our nonconcentric Pd−Au NPs can provide superior catalytic performance to that of the alloyed NPs. For example, although the Pd−Au_{20} NPs show a similar H_2O_2 selectivity to that of the alloyed $Pd_{50}Au_{50}$ NPs, their catalytic activity (H_2O_2 productivity and H_2 conversion) is higher than those of the alloyed structures. With the Pd−Au_{30} catalysts, one can achieve a selectivity of almost 100%, although the H_2 conversion is not significantly lower than that of the alloyed structures. From these results, it is found that both the exposed Pd domains and Pd−Au alloyed domains are required to increase H_2 conversion and H_2O_2 selectivity, respectively, which indicates the potential of nonconcentric Pd−Au NP catalysts that include both domains.

Thus, far, we have shown that nonconcentric Pd−Au NPs have excellent catalytic performance in direct H_2O_2 synthesis; however, their growth mechanism at the atomic level is still unclear. In particular, the following questions were raised: (1) How can Au atoms grow locally on only one or several surfaces instead of fully covering all the surfaces of a Pd seed? (2) Why does the number of Au shells depend on the amount of Au precursor? To answer these questions, additional experiments were performed by manipulating two variables, the reaction time and the concentration of the Au precursor.

To observe nucleation and growth of the Au shells on the Pd seeds, we investigated the effects of the reaction time from 1 to 15 min at a constant concentration of Au precursors (1 wt %)

https://doi.org/10.1021/acs.jpclett.1c03256
J. Phys. Chem. Lett. 2021, 12, 11098−11105

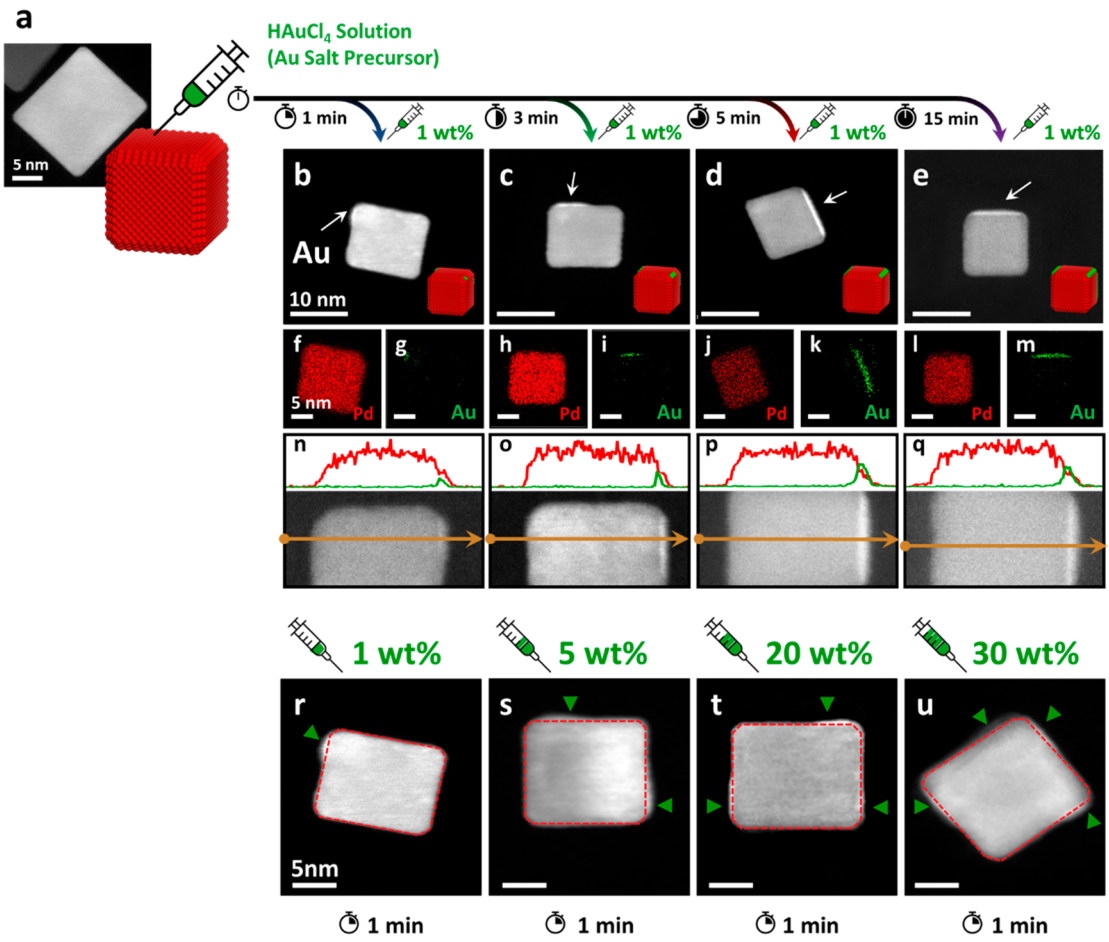

Figure 2. Nucleation and growth behaviors of the nonconcentric Pd–Au NPs. (a) TEM image of a Pd nanocube. (b–e) TEM images of the Pd–Au NPs synthesized with a constant concentration of 1 wt % Au precursor for several reaction times of 1 min (b), 3 min (c), 5 min (d), and 15 min (e). In panels a–e, each atomic structure is also included. (f–m) EDS mapping images of the nonconcentric Pd–Au NPs, in which Pd = red and Au = green. (n–q) EDS line scanned images (red, Pd; green, Au). (r–u) TEM images of the Pd–Au NPs synthesized by controlling Au precursor concentrations with 1 (r), 5 (s), 20 (t), and 30 wt % (u) in which a very short reaction time (~1 min) was considered. The green arrows indicate the nucleation positions of the Au atoms.

(Figure 2a–q). Nucleation of Au atoms (brighter atoms) was initiated near corners of the Pd seeds (Figure 2b). Longer reaction times led to gradual growth of the nucleated Au shell along a Pd facet adjacent to the nucleation sites (Figure 2c–e). In particular, after a reaction time of 5 min, it appeared that the Au layer fully covered one facet of the Pd seed. These results are supported by the EDS mapping images (Figure 2f–m). We carried out EDS line scanning analyses for the Pd NPs with Au shells to scrutinize the atomic distributions near the interfaces between the Pd seeds and the formed Au shells (Figure 2n–q) and found that the Pd and Au signals coexist near the interfaces, which implies the possibility that Pd and Au atoms are alloyed. The details will be further discussed later in this work. We also investigated the effects of the Au precursor concentration, and a short reaction time of 1 min was used to clarify the nucleation behaviors. In Figure 2r–u, the HAADF–STEM images clearly show that as the concentration of the Au precursor increased, the number of Au nucleation sites on the Pd seed increased, which supports the findings shown in Figure 1a–h that the shape of nonconcentric NPs (the number of Au shells grown on Pd seeds) is controlled via the concentration of the Au precursor. Moreover, Au atoms were preferentially deposited near the corners of Pd seeds regardless of the concentration of the Au precursor. Lattice-resolved high-resolution scanning transmission electron microscopy (STEM) also reveals that the Au layers grew over onto the (100) facets of the Pd seed (Figure S3, Supporting Information), as previously shown in Figure 1a–h. Despite careful analyses using TEM, EDS, and STEM, several questions still remain to be answered:

(i) In the early stage of Au shell formation, why do Au atoms preferentially nucleate at the corners of the Pd seeds? (Figure S4a, Supporting Information)

(ii) It seems that Au experiences overgrowth along the Pd(100) surfaces after nucleation. Why does Au prefer to grow on the Pd(100) surfaces over other surfaces? (Figure S4b, Supporting Information)

(iii) Does the newly formed shell indeed consist of pure Au layers without alloying with Pd? What is the thermodynamically stable atomic distribution in the newly formed shells? (Figure S4c, Supporting Information)

To answer these questions, we additionally performed DFT calculations.

For the first question, we calculated the adsorption energy of a Au atom (E_{ads}) on the (100), (110), and (111) surfaces of Pd by DFT, in which the adsorption behaviors on the interface

https://doi.org/10.1021/acs.jpclett.1c03256
J. Phys. Chem. Lett. 2021, 12, 11098–11105

between Pd(100) and Pd(110) surfaces were additionally considered to further model the NP structure (Figure 3). The E_{ads} is defined as follows:

$$E_{ads} = E_{tot} - [E_{clean\text{-}Pd} + E_{Au}] \quad (1)$$

E_{tot}, $E_{clean\text{-}Pd}$, and E_{Au} are the total energies of each Pd surface with adsorbed Au atom(s), of clean Pd surfaces, and of a free Au atom, respectively. By definition, a lower E_{ads} indicates stronger adsorption on the Pd surface. Among them, the most favorable adsorption site for Au is the fcc site on Pd(110), which has an adsorption energy of −3.47 eV; this value is obviously lower than those on the (100) and (111) surfaces. This result clearly reveals that a Au atom prefers to nucleate on the Pd(110) surfaces. It was also found that the second Au atom prefers to adsorb on the Pd(110) surface but is positioned closer to the (110)/(100) interface, implying the possibility that additional Au atoms likely enable overgrowth toward the (100) surfaces. Figure S5 obviously shows the Au nucleation trends. In an early stage, Au atoms prefer to adsorb on Pd(110) closer to the (110)/(100) interfaces in Figure S5a−g. However, when Pd(110) is fully covered with Au atoms (Figure S5g), the preferred Au adsorption sites are changed to the (100) facet.

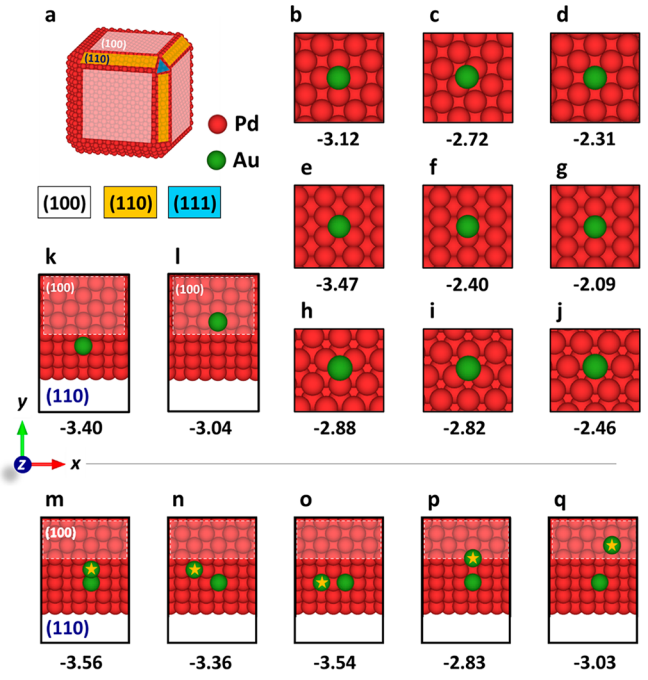

Figure 3. DFT adsorption energies of (a−l) one or (m−q) two Au atom(s) on the Pd(100), (110), and (111) surfaces. (a) Schematic atomic structure of the Pd nanocube. Adsorption energies of one Au atom on the (b−d) Pd(100), (e−g) Pd(110), (h−j) Pd(111), and (k−l) Pd(100)/(110) interfaces. (m−q) Green circle with yellow star symbol indicates newly adsorbed Au atom position candidates based on the panel k structure.

To answer the second question, we define the shell formation energy (E_{sh}) as follows:

$$E_{sh} = E_{tot} - E_{Pd\text{-}slab} - N\mu_{Au} \quad (2)$$

E_{tot} is the total energy of a Pd−Au system, $E_{Pd\text{-}slab}$ is the total energy of a Pd slab including the same number of Pd atoms as that of the Pd−Au system, μ_{Au} is the cohesive energy of Au, and N is the number of Au atoms in the given system. According to the definition, a lower E_{sh} indicates a more thermodynamically stable shell. By comparing the E_{sh} values for the Pd−Au systems (Au atoms or layers on Pd(100), Pd(110), or Pd(111) surfaces), one can determine the Pd surface on which the Au atoms grow preferentially. For comparison, we also calculated the E_{sh} for atomic Au deposited on Pd slabs. Thus, we compared the E_{sh} of the Pd−Au core−shell slab systems with those of atomic or layered Au shells (1−3 layers) (Figure 4). Here, shell candidates were obtained from the most stable adsorption sites of Au on each Pd slab. For atomic Au (Figure 4a−c), the Pd(110) surface had the lowest E_{sh} and the only negative value among several surfaces; this result also supports that the nucleation of Au shells on Pd nanocubes occurs preferentially on the Pd(110) over other surfaces, as illustrated in Figure 3. However, for layered Au (Figure 4d−f), the trend changes; the Pd(100) surface has the lowest E_{sh} values irrespective of the number of Au layers. From these results, it was found that although Au nuclei are preferentially generated on Pd(110), the Au shell or layer growth resulting from additional deposition of Au atoms is thermodynamically more favorable on Pd(100). Before the Au nuclei fully cover the Pd(110) surfaces, the Au atoms likely start to grow over onto the Pd(100) surface, which is confirmed by comparing the E_{sh} values of one Au layer.

To elucidate the atomic distributions near the interfaces between the Pd nanocubes and the newly formed shells (the third question), we additionally calculated the E_{sh} of various shell structures on Pd(100) slabs, as shown in Figure 4. In this calculation, Pd slabs with 4 layers were modeled with 32 Pd atoms (8 atoms per layer). When 8 Au atoms were deposited on the Pd slabs (Figure 4g−j), the structure with one Au layer fully covering the Pd slab was the most thermodynamically favorable (Figure 4g), similar to the Pd−Au core−shell structure. However, when 16 Au atoms were added (Figure 4k−n), the Pd−Au core−shell structures with 2 Au layers were no longer the most favorable structures. Instead, the atomic distribution in which the top surface layer consisted of only Au atoms and the Au and Pd atoms were alloyed in the subsurface (Figure 4l) is more stable. When more Au atoms (24 atoms) were deposited, as shown in Figure 4o−v, a similar behavior was observed. Because Pd and Au crystals have a lattice mismatch of ∼4.5%, the Pd−Au core−shell structures can have high lattice strains. However, the high lattice strain can be relieved by the formation of the Pd−Au alloyed structure because the lattice parameters of the alloyed structures are between the lattice parameters of the Pd and Au crystals. From these results, it is concluded that alloyed structures of Pd and Au formed between the Pd nanocubes and the Au shells; this conclusion is also supported by the STEM-EDS line scanning analysis shown in Figure 2n−q. As a result, due to the formation of the Pd−Au alloyed regions, the nonconcentric Pd−Au NPs can provide superior H_2O_2 selectivity. Based on the results explained thus far, the formation process of the nonconcentric Pd−Au NPs is schematically represented in Figure S6.

In the field of multimetallic catalysis for H_2O_2 synthesis, state-of-the-art catalysts with core@shell or alloyed structures still face limitations in enhancing both the catalytic activity and selectivity. As a plausible exit strategy to overcome this limitation, we suggest nonconcentric Pd−Au NPs with all three types of Pd- and Au-domains and Pd−Au interfaces in one structure (3-in-1 strategy). In particular, the nonconcentric Pd−Au_{20} NPs show balanced harmony between the Pd

https://doi.org/10.1021/acs.jpclett.1c03256
J. Phys. Chem. Lett. 2021, 12, 11098−11105

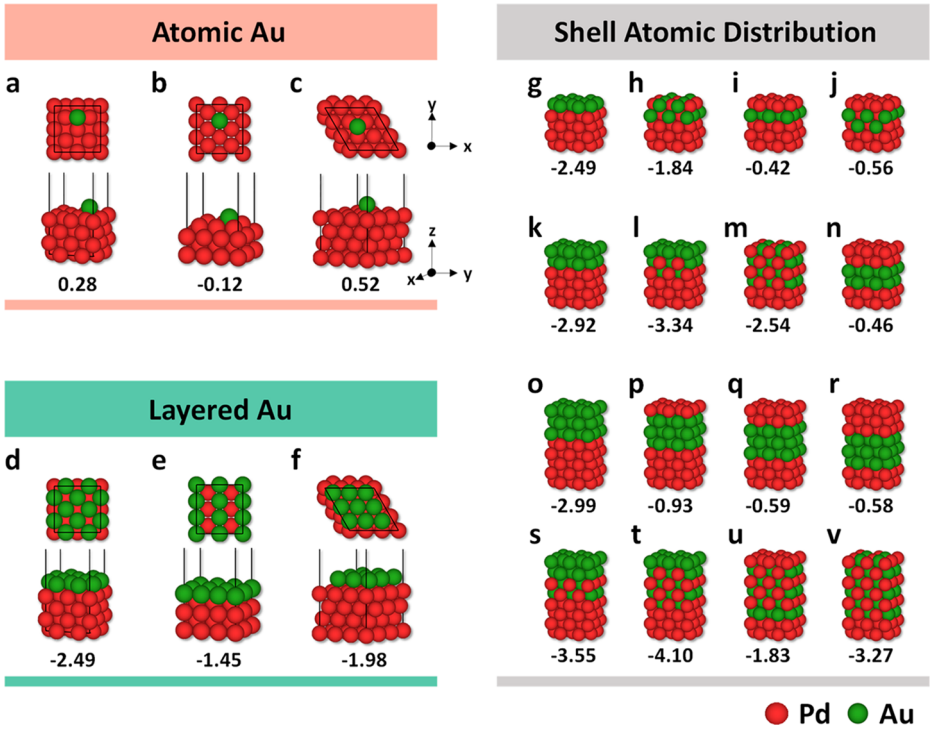

Figure 4. DFT-calculated formation energies (eV) of the atomic (a–c), layered Au (d–f), and shell atomic distribution (g–v) of the Pd–Au slabs. Atomic Au models are Au atoms adsorbed on Pd(100) (a), Pd(110) (b), and Pd(111) (c) slabs. Layered Au models are fully covered with a Au layer on the Pd(100) (d), Pd(110) (e), and Pd(111) (f) slabs. To model the atomic distribution of the shell, 32 Pd atoms were used in the Pd(100) slab models, including (g–j) 8 Au atoms, (k–n) 16 Au atoms, and (o–v) 24 Au atoms.

domain and Pd–Au interfaces and provide both superior catalytic selectivity and activity. Moreover, the formation mechanism of the nonconcentric Pd–Au NPs was elucidated at the atomic scale by a comprehensive combination of TEM characterization and DFT calculations. This study readily provides a new category (nonconcentric structure) in the field of multimetallic NP catalysts, and this 3-in-1 strategy can be applied to various catalysis fields to simultaneously enhance the activity and selectivity.

EXPERIMENTAL METHODS

Chemicals. Poly(vinyl pyrrolidone) (PVP, MW 55 000), L-ascorbic acid (AA), potassium bromide (KBr), sodium tetrachloropalladate (Na_2PdCl_4), and gold chloride hydrate ($HAuCl_4{\cdot}xH_2O$) were purchased from Sigma-Aldrich.

Nanoparticle Synthesis. To fabricate the Pd–Au_N nanoparticles, 37 mg of PVP, 50 mg of AA, and 300 mg of KBr were dissolved in 8 mL of deionized (DI) water and heated at 80 °C for 20 min. One milliliter of DI water with 57 mg of Na_2PdCl_4 was injected into the reaction solution. After 3 h, an additional 0.5 mL of DI water with 73 mg of AA was added, and then $HAuCl_4{\cdot}xH_2O$ (0.72, 3.58, 14.30, or 21.45 mg for nonconcentric Pd–Au_1, Pd–Au_5, Pd–Au_{20}, and Pd–Au_{30}, respectively) in 1 mL of DI water was rapidly injected into the reaction solution. After 15 min, the reaction solution was washed with acetone and dispersed in DI water. For Pd seeds, a synthetic procedure was conducted under the same experimental conditions without additional AA and $HAuCl_4{\cdot}xH_2O$ solutions.

Characterization. Transmission electron microscopy (TEM) images and energy-dispersive X-ray spectra (EDS) were acquired using a transmission electron microscope (FEI Talos F200X) equipped with scanning transmission electron microscopy/energy dispersive X-ray spectroscopy (Bruker Super-X EDS system). The crystal structure was examined by X-ray diffraction (Rigaku Dmax 2500 and Smartlab) with Cu Kα radiation (λ = 1.54 Å). The samples used to obtain the TEM images and XRD spectra were purified by centrifugation three times to remove surfactants and excess reactants. Then, the NPs were dispersed in DI water.

Computation. All DFT calculations were performed using the Vienna Ab Initio Simulation Packages (VASP)[34] using the projector-augmented-wave (PAW)[35] method to describe the potential from the ionic core. For the exchange and correlation terms, we employed the revised Perdew–Burke–Ernzerhof (RPBE) functional.[36] An energy cutoff of 480 eV and Monkhorst–Pack k-point meshes of 8 × 8 × 8 and 3 × 3 × 1 were used for the bulk and slab calculations, respectively, after an extensive convergence test. A large vacuum spacing of 15 Å was used to prevent interslab interactions. The Pd(100) and Pd(110) surfaces and Pd(100)/(110) interface were modeled by supercell slabs that consisted of 4 × 4 and 6 × 8 surface unit cells with four layers and six layers, respectively, for shell formation energy calculations. While the bottom two layers in the Pd slabs were fixed, the top two layers and the reactant molecules were optimized until the energy change was less than 1×10^{-4} eV/cell and the force on each atom was less than 0.02 eV $Å^{-1}$. The surface incorporation of Au atoms on Pd is strongly influenced by the compressive stress on Au surface atoms. This stress has been shown to cause structural transitions in experimentally observed nanoparticles at equilibrium.[18] For more realistic simulation of the shell layers, DFT calculations were performed with the Pd/Au slab model in which the Au surface atoms were compressed because the bottom two layers in the Pd slab were fixed.

https://doi.org/10.1021/acs.jpclett.1c03256
J. Phys. Chem. Lett. 2021, 12, 11098–11105

Catalytic Performance Measurements. Catalytic direct H_2O_2 synthesis reactions were performed in a double-jacketed glass reactor under continuous stirring at 1200 rpm. For H_2O_2 synthesis, the reaction medium (total of 150 mL) was DI water containing 20 vol % ethanol and 3.0×10^{-2} M H_3PO_4. The amount of the SiO_2-supported Pd−Au_N nanoparticles used was fixed at 0.35 mg. In terms of safety, the explosion limitation of H_2 in the H_2/O_2 mixture was less than 4 mol % or more than 95.2 mol %.[37] Thus, to avoid contact between the dry catalysts and the H_2/O_2 gas, the reaction medium saturated with H_2 and O_2 gas was mixed with the powdered catalysts to form a slurry. Then, the suspension, which included the catalyst, was injected back into the reactor. The flow rate of the reactant gas stream was 22 mL/min (volumetric ratio of H_2/O_2 = 1:10), and the reaction was performed at 10 °C and 1 atm for 0.5 h. After the reaction, the H_2O_2 concentration was measured by iodometric titration. H_2 conversion was calculated from H_2 concentration data measured by gas chromatography (Carboxen 1000 packed column, SUPELCO). Equations 3, 4, and 5 were used to calculate the H_2 conversion, H_2O_2 selectivity, and H_2O_2 production rate,[38] respectively:

$$\text{H}_2\text{ conversion (\%)} = \frac{\text{total moles of H}_2\text{ reacted}}{\text{total moles of H}_2\text{ fed}} \times 100 \quad (3)$$

$$\text{H}_2\text{O}_2\text{ selectivity (\%)} = \frac{\text{moles of H}_2\text{O}_2\text{ generated}}{\text{total moles of H}_2\text{ reacted}} \times 100 \quad (4)$$

$$\text{H}_2\text{O}_2\text{ production rate}\left(\frac{\text{mmol H}_2\text{O}_2}{g_{\text{metal}} \times h}\right) = \frac{\text{mmol of H}_2\text{O}_2\text{ generated}}{\text{weight of metal (g) in used catalyst} \times \text{reaction time (h)}} \quad (5)$$

■ ASSOCIATED CONTENT

Supporting Information

The Supporting Information is available free of charge at https://pubs.acs.org/doi/10.1021/acs.jpclett.1c03256.

Presynthesized Pd nanocubes, XRD patterns, HR-STEM images, several mechanistic questions, adsorption energies of several Au atoms on the Pd(100)/(110) interfaces, answers for nucleation, growth and shell atomic distribution of Pd−Au NPs, and catalytic performance of nonconcentric Pd−Au NPs (PDF)

■ AUTHOR INFORMATION

Corresponding Authors

Kwan-Young Lee − *Department of Chemical and Biological Engineering, Korea University, Seoul 02841, Republic of Korea;* orcid.org/0000-0002-5637-1009; Email: kylee@korea.ac.kr

Sang Soo Han − *Computational Science Research Center, Korea Institute of Science and Technology, Seoul 02792, Republic of Korea;* orcid.org/0000-0002-7925-8105; Email: sangsoo@kist.re.kr

Taekyung Yu − *Department of Chemical Engineering, Integrated Engineering Major, Kyung Hee University, Yongin 17104, Republic of Korea;* orcid.org/0000-0003-4703-3523; Email: tkyu@khu.ac.kr

Authors

Hong Woo Lee − *Computational Science Research Center, Korea Institute of Science and Technology, Seoul 02792, Republic of Korea; Department of Chemical and Biological Engineering, Korea University, Seoul 02841, Republic of Korea*

Euiyoung Jung − *Department of Chemical Engineering, Integrated Engineering Major, Kyung Hee University, Yongin 17104, Republic of Korea*

Geun-Ho Han − *Department of Chemical and Biological Engineering, Korea University, Seoul 02841, Republic of Korea;* orcid.org/0000-0002-8949-4777

Min-Cheol Kim − *Computational Science Research Center, Korea Institute of Science and Technology, Seoul 02792, Republic of Korea;* orcid.org/0000-0002-4457-7421

Donghun Kim − *Computational Science Research Center, Korea Institute of Science and Technology, Seoul 02792, Republic of Korea;* orcid.org/0000-0003-0326-5381

Complete contact information is available at: https://pubs.acs.org/10.1021/acs.jpclett.1c03256

Author Contributions

▽H.W.L., E.J., and G.-H.H. contributed equally.

Notes

The authors declare no competing financial interest.

■ ACKNOWLEDGMENTS

This work was supported by the Creative Materials Discovery Program through the National Research Foundation of Korea (NRF-2016M3D1A1021141).

■ REFERENCES

(1) Sankar, M.; Dimitratos, N.; Miedziak, P. J.; Wells, P. P.; Kiely, C. J.; Hutchings, G. J. Designing Bimetallic Catalysts for a Green and Sustainable Future. *Chem. Soc. Rev.* **2012**, *41*, 8099−8139.

(2) Gilroy, K. D.; Ruditskiy, A.; Peng, H.-C.; Qin, D.; Xia, Y. Bimetallic Nanocrystals: Syntheses, Properties, and Applications. *Chem. Rev.* **2016**, *116*, 10414−10472.

(3) Loza, K.; Heggen, M.; Epple, M. Synthesis, Structure, Properties, and Applications of Bimetallic Nanoparticles of Noble Metals. *Adv. Funct. Mater.* **2020**, *30*, 1909260.

(4) Marakatti, V. S.; Peter, S. C. Synthetically Tuned Electronic and Geometrical Properties of Intermetallic Compounds as Effective Heterogeneous Catalysts. *Prog. Solid State Chem.* **2018**, *52*, 1−30.

(5) Wang, C.; Markovic, N. M.; Stamenkovic, V. R. Advanced Platinum Alloy Electrocatalysts for the Oxygen Reduction Reaction. *ACS Catal.* **2012**, *2*, 891−898.

(6) Zhang, E.; Ma, F.; Liu, J.; Sun, J.; Chen, W.; Rong, H.; Zhu, X.; Liu, J.; Xu, M.; Zhuang, Z.; Chen, S.; Wen, Z.; Zhang, J. Porous Platinum−Silver Bimetallic Alloys: Surface Composition and Strain Tunability Toward Enhanced Electrocatalysis. *Nanoscale* **2018**, *10*, 21703−21711.

(7) Kobayashi, H.; Kusada, K.; Kitagawa, H. Creation of Novel Solid-Solution Alloy Nanoparticles on the Basis of Density-of-States Engineering By Interelement Fusion. *Acc. Chem. Res.* **2015**, *48*, 1551−1559.

(8) Strasser, P.; Koh, S.; Anniyev, T.; Greeley, J.; More, K.; Yu, C.; Liu, Z.; Kaya, S.; Nordlund, D.; Ogasawara, H.; Toney, M. F.; Nilsson, A. Lattice-Strain Control of the Activity in Dealloyed Core−Shell Fuel Cell Catalysts. *Nat. Chem.* **2010**, *2*, 454−460.

(9) Gamler, J. T. L.; Leonardi, A.; Sang, X.; Koczkur, K. M.; Unocic, R. R.; Engel, M.; Skrabalak, S. E. Effect of Lattice Mismatch and Shell Thickness on Strain in Core@Shell Nanocrystals. *Nanoscale Adv.* **2020**, *2*, 1105−1114.

(10) Xu, J.; Wilson, A. R.; Rathmell, A. R.; Howe, J.; Chi, M.; Wiley, B. J. Synthesis and Catalytic Properties of Au−Pd Nanoflowers. *ACS Nano* **2011**, *5*, 6119−6127.
(11) Qiu, J.; Xie, M.; Lyu, Z.; Gilroy, K. D.; Liu, H.; Xia, Y. General Approach to the Synthesis of Heterodimers of Metal Nanoparticles through Site-Selected Protection and Growth. *Nano Lett.* **2019**, *19*, 6703−6708.
(12) Edwards, J. K.; Hutchings, G. J. Palladium and Gold−Palladium Catalysts for the Direct Synthesis of Hydrogen Peroxide. *Angew. Chem., Int. Ed.* **2008**, *47*, 9192−9198.
(13) Edwards, J. K.; Solsona, B.; N, E. N.; Carley, A. F.; Herzing, A. A.; Kiely, C. J.; Hutchings, G. J. Switching Off Hydrogen Peroxide Hydrogenation in the Direct Synthesis Process. *Science* **2009**, *323*, 1037−1041.
(14) Han, Y.-F.; Zhong, Z.; Ramesh, K.; Chen, F.; Chen, L.; White, T.; Tay, Q.; Yaakub, S. N.; Wang, Z. Au Promotional Effects on the Synthesis of H2O2 Directly from H2 and O2 on Supported Pd−Au Alloy Catalysts. *J. Phys. Chem. C* **2007**, *111*, 8410−8413.
(15) Ricciardulli, T.; Gorthy, S.; Adams, J. S.; Thompson, C.; Karim, A. M.; Neurock, M.; Flaherty, D. W. Effect of Pd Coordination and Isolation on the Catalytic Reduction of O2 To H2O2 over PdAu Bimetallic Nanoparticles. *J. Am. Chem. Soc.* **2021**, *143*, 5445−5464.
(16) Corbos, E. C.; Ellis, P. R.; Cookson, J.; Briois, V.; Hyde, T. I.; Sankar, G.; Bishop, P. T. Tuning the Properties of PdAu Bimetallic Nanocatalysts for Selective Hydrogenation Reactions. *Catal. Sci. Technol.* **2013**, *3*, 2934−2943.
(17) Zhu, C.; Zeng, J.; Tao, J.; Johnson, M. C.; Schmidt-Krey, I.; Blubaugh, L.; Zhu, Y.; Gu, Z.; Xia, Y. Kinetically Controlled Overgrowth of Ag or Au on Pd Nanocrystal Seeds: From Hybrid Dimers to Nonconcentric and Concentric Bimetallic Nanocrystals. *J. Am. Chem. Soc.* **2012**, *134*, 15822−15831.
(18) Nelli, D.; Roncaglia, C.; Ferrando, R.; Minnai, C. Shape Changes in AuPd Alloy Nanoparticles Controlled by Anisotropic Surface Stress Relaxation. *J. Phys. Chem. Lett.* **2021**, *12*, 4609−4615.
(19) Bochicchio, D.; Ferrando, R. Morphological Instability of Core-Shell Metallic Nanoparticles. *Phys. Rev. B: Condens. Matter Mater. Phys.* **2013**, *87*, 165435.
(20) Ferrando, R. Symmetry Breaking and Morphological Instabilities in Core-Shell Metallic Nanoparticles. *J. Phys.: Condens. Matter* **2015**, *27*, 013003.
(21) Lee, H. W.; Nam, H.; Han, G.-H.; Cho, Y.-H.; Yeo, B. C.; Kim, M.-C.; Kim, D.; Lee, K.-Y.; Lee, S. Y.; Han, S. S. Solid-Solution Alloying of Immiscible Pt and Au Boosts Catalytic Performance for H2O2 Direct Synthesis. *Acta Mater.* **2021**, *205*, 116563.
(22) Flaherty, D. W. Direct Synthesis of H2O2 from H2 and O2 on Pd Catalysts: Current Understanding, Outstanding Questions, and Research Needs. *ACS Catal.* **2018**, *8*, 1520−1527.
(23) Xu, Y.; Mavrikakis, M. Adsorption and Dissociation of O2 on Gold Surfaces: Effect of Steps and Strain. *J. Phys. Chem. B* **2003**, *107*, 9298−9307.
(24) Han, G.-H.; Lee, S.-H.; Hwang, S.-Y.; Lee, K.-Y. Advanced Development Strategy of Nano Catalyst and DFT Calculations for Direct Synthesis of Hydrogen Peroxide. *Adv. Energy Mater.* **2021**, *11*, 2003121.
(25) Chen, L.; Medlin, J. W.; Grönbeck, H. On the Reaction Mechanism of Direct H2O2 Formation over Pd Catalysts. *ACS Catal.* **2021**, *11*, 2735−2745.
(26) Jin, M.; Liu, H.; Zhang, H.; Xie, Z.; Liu, J.; Xia, Y. Synthesis of Pd Nanocrystals Enclosed by {100} Facets and with Sizes < 10 nm for Application in CO Oxidation. *Nano Res.* **2011**, *4*, 83−91.
(27) Lu, X.; Tuan, H.-Y.; Korgel, B. A.; Xia, Y. Facile Synthesis of Gold Nanoparticles with Narrow Size Distribution by Using AuCl or AuBr as the Precursor. *Chem. - Eur. J.* **2008**, *14*, 1584−1591.
(28) Garg, N.; Scholl, C.; Mohanty, A.; Jin, R. The Role of Bromide Ions in Seeding Growth of Au Nanorods. *Langmuir* **2010**, *26*, 10271−10276.
(29) Kim, I.; Seo, M.-G.; Choi, C.; Kim, J. S.; Jung, E.; Han, G.-H.; Lee, J.-C.; Han, S. S.; Ahn, J.-P.; Jung, Y.; Lee, K.-Y.; Yu, T. Studies on Catalytic Activity of Hydrogen Peroxide Generation according to Au Shell Thickness of Pd/Au Nanocubes. *ACS Appl. Mater. Interfaces* **2018**, *10*, 38109−38116.
(30) Wilson, N. M.; Priyadarshini, P.; Kunz, S.; Flaherty, D. W. Direct Synthesis of H2O2 on Pd and AuxPd1 Clusters: Understanding the Effects of Alloying Pd with Au. *J. Catal.* **2018**, *357*, 163−175.
(31) Li, J.; Ishihara, T.; Yoshizawa, K. Theoretical Revisit of the Direct Synthesis of H2O2 on Pd and Au@Pd Surfaces: A Comprehensive Mechanistic Study. *J. Phys. Chem. C* **2011**, *115*, 25359−25367.
(32) Kim, J.-S.; Kim, H.-K.; Kim, S.-H.; Kim, I.; Yu, T.; Han, G.-H.; Lee, K.-Y.; Lee, J.-C.; Ahn, J.-P. Catalytically Active Au Layers Grown on Pd Nanoparticles for Direct Synthesis of H2O2: Lattice Strain and Charge-Transfer Perspective Analyses. *ACS Nano* **2019**, *13*, 4761−4770.
(33) Sankar, M.; He, Q.; Morad, M.; Pritchard, J.; Freakley, S. J.; Edwards, J. K.; Taylor, S. H.; Morgan, D. J.; Carley, A. F.; Knight, D. W.; Kiely, C. J.; Hutchings, G. J. Synthesis of Stable Ligand-Free Gold−Palladium Nanoparticles Using a Simple Excess Anion Method. *ACS Nano* **2012**, *6*, 6600−6613.
(34) Kresse, G.; Furthmüller, J. Efficiency of Ab-Initio Total Energy Calculations for Metals and Semiconductors Using a Plane-Wave Basis Set. *Comput. Mater. Sci.* **1996**, *6*, 15−50.
(35) Kresse, G.; Joubert, D. From Ultrasoft Pseudopotentials to the Projector Augmented-Wave Method. *Phys. Rev. B: Condens. Matter Mater. Phys.* **1999**, *59*, 1758−1775.
(36) Hammer, B.; Hansen, L. B.; Nørskov, J. K. Improved Adsorption Energetics within Density-Functional Theory Using Revised Perdew-Burke-Ernzerh of Functionals. *Phys. Rev. B: Condens. Matter Mater. Phys.* **1999**, *59*, 7413−7421.
(37) Vu, H. T. T.; Vo, V. L. L.; Chung, Y.-M. Direct Synthesis of Hydrogen Peroxide over Palladium Catalysts Supported on Glucose-Derived Amorphous Carbons. *Korean J. Chem. Eng.* **2021**, *38*, 1139−1148.
(38) Hang, V. T. T.; Chung, Y.-M. Direct Synthesis of H2O2 over Pd/C Catalysts Prepared by the Incipient Wetness. *Korean J. Chem. Eng.* **2020**, *37*, 65−71.

https://doi.org/10.1021/acs.jpclett.1c03256
J. Phys. Chem. Lett. 2021, 12, 11098−11105